Charge Puddles in Graphene near the Dirac Point

S. Samaddar,[1,2] I. Yudhistira,[3] S. Adam,[3,4] H. Courtois,[1,2] and C. B. Winkelmann[1,2,*]
[1]Université Grenoble Alpes, Institut NEEL, F-38042 Grenoble, France
[2]CNRS, Institut NEEL, F-38042 Grenoble, France
[3]Centre for Advanced 2D Materials and Department of Physics, National University of Singapore, 2 Science Drive 3, Singapore 117551, Singapore
[4]Yale-NUS College, 16 College Avenue West, Singapore 138527, Singapore

(Received 17 December 2015; published 23 March 2016)

The charge carrier density in graphene on a dielectric substrate such as SiO_2 displays inhomogeneities, the so-called charge puddles. Because of the linear dispersion relation in monolayer graphene, the puddles are predicted to grow near charge neutrality, a markedly distinct property from conventional two-dimensional electron gases. By performing scanning tunneling microscopy and spectroscopy on a mesoscopic graphene device, we directly observe the puddles' growth, both in spatial extent and in amplitude, as the Fermi level approaches the Dirac point. Self-consistent screening theory provides a unified description of both the macroscopic transport properties and the microscopically observed charge disorder.

DOI: 10.1103/PhysRevLett.116.126804

Electrons in graphene are subjected to a disordered potential created by random charged impurities, either adsorbed on the graphene or buried in the substrate. These lead to inhomogeneities in the local carrier density, that is, charge puddles [1–7]. Scanning probe microscopies have, in particular, strongly contributed to unraveling the puddles' spatial properties and have challenged different theories about their origin [1–3]. Charge puddles are usually thought of as a limitation to the extent the charge neutrality point can be approached macroscopically, thereby also limiting possible device performances. However, the behavior of the puddles themselves unveils the fascinating electronic properties of graphene and, more generally, Dirac materials.

Electrostatic screening in two dimensions has a counterintuitive behavior. Thomas-Fermi screening entails a characteristic length scale q_{TF}^{-1}. Unlike in three dimensions, the Thomas-Fermi wave vector q_{TF} in a 2D electron gas (2DEG) is proportional to the density of states at the Fermi level. As a consequence, q_{TF} is energy and thus carrier density independent in conventional 2DEGs, while q_{TF} is proportional to $k_F = \sqrt{\pi n}$ in graphene and other Dirac materials. This has the important consequence that the unscreened potential created by a charged impurity in a medium with dielectric constant κ, $V(q) = e^2/2\kappa\epsilon_0 q$, and the screened potential $\tilde{V}(q) \propto (q + q_{\mathrm{TF}})^{-1}$ are identical within a multiplicative constant [7]. In other words, near charge neutrality local inhomogeneities in the screened potential can be arbitrarily large. Further, a rough estimate of the lateral extent of charge carrier density correlations is given by q_{TF}^{-1}, from which a strong growth $\propto 1/\sqrt{n}$ of the puddles' size is expected near charge neutrality. The carrier density dependence of both the charge puddles' amplitude and size in a Dirac material has not yet been reported.

In this Letter, we report the direct microscopic observation of the doping disorder landscape in monolayer graphene at different charge carrier densities. The charge inhomogeneities are found to grow, both in spatial extent and in amplitude, as the Fermi level approaches the Dirac point. From transport measurements on the very same graphene sample at study, the microscopic parameters of the disorder potential can be estimated in the frame of the self-consistent screening theory. Calculations of the charge puddles' distribution based on these are in very good agreement with the experimental observations.

The sample is fabricated on a heavily doped Si substrate covered with thermal oxide. Single layer graphene is prepared by mechanical exfoliation [8]. The number of graphene layers and the absence of surface contamination are confirmed from combined optical, Raman, and *ex situ* AFM characterization. Using a mechanical mask [9], we deposit the metallic source and drain contacts to form a 4 μm long graphene junction [Fig. 1(a)]. Organic resist is avoided, as to ensure a residue-free surface for scanning probe microscopy. Details of the device fabrication are described in the Supplemental Material [10].

The experimental setup is a homemade combined AFM-STM operating at a temperature of 130 mK [21], at which all measurements presented here were obtained. The sample stage allows for *in situ* multiterminal transport measurements of the device. AFM is performed by electrical excitation and readout of a mechanical quartz length extension resonator [22,23]. This allows us to rapidly move the tip to the graphene junction with the help of the position code [24,25]. Scanning tunneling micrographs reveal a clean graphene surface, following the substrate corrugation with a roughness of about 100 pm (see Supplemental Material file for details [10]). Scanning tunneling spectroscopy is achieved

 © 2016 American Physical Society

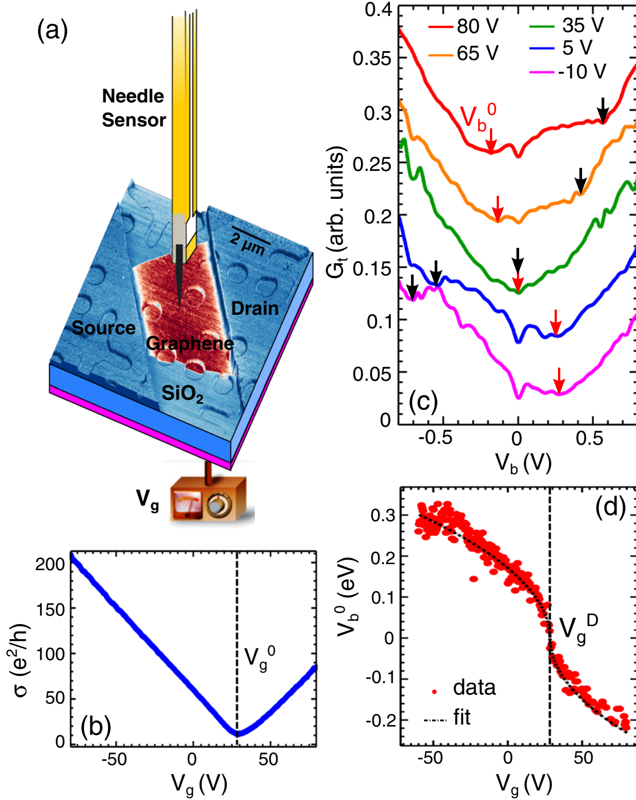

FIG. 1. (a) Experimental configuration, combining transport measurements with scanning probe microscopy on a monolayer graphene device. A conductive tip mounted on a stiff mechanical resonator serves as the probe for combined AFM-STM. Two isolated electrical contacts (*Source* and *Drain*) enable two-probe transport measurements. The atomic force micrograph shows both the topography (vertical scale, varying between 0 and 57 nm) and the phase (varying by 3.8° from blue to brown). (b) Device conductivity as a function of back-gate voltage V_g, measured at a bias voltage of 5 mV. The overall charge neutrality point is found at $V_g^0 = 29$ V. (c) Differential tip-to-sample tunneling conductance G_t as a function of the voltage V_b (uniformly applied to the sample), at several values of V_g. The red and black arrows indicate the position of the primary (V_b^0) and the secondary minimum of G_t, respectively (see text). $I_t^{\text{set}} = 50$ pA at $V_b = 0.9$ V. The curves are vertically offset for clarity. (d) Variation of the primary minimum with V_g. The black dashed line shows the fit with Eq. (1), yielding the fit parameter $V_g^D = 28$ V.

by lock-in measurements of the differential tip-to-sample tunneling conductance $G_t(x, y) = dI_t/dV_b$, by adding a 12 mV ac modulation at frequency $f = 322$ Hz to the bias voltage V_b, which is uniformly applied to the sample.

Transport measurements are performed with the tip retracted a few hundred nm from the sample surface. However, approaching the tip to STM contact does not produce a significant effect in the device characteristics. The conductivity of the graphene device shows a perfectly linear behavior at high carrier densities [Fig. 1(b)], in line with a density-independent mobility of about 6000 cm^2 V^{-1} s^{-1}. This indicates that carrier transport is dominated by long-range disorder, as can be caused by random charge impurities in the substrate [26]. A slight difference between the measured electron and hole mobilities, $\mu_e/\mu_h = 0.9 \pm 0.05$, could be related to the difference in their scattering cross sections off charged impurities [5,27].

The gate voltage at which conductivity is minimized gives the overall charge neutrality point, $V_g^0 = 29$ V. This overall hole doping is consistent with the presence of negatively charged silanol groups on the surface. A residual conductivity $\sigma_0 \approx 11e^2/h$ is found at the charge neutrality point. Within self-consistent screening theory [7], the above values of residual conductivity and mobility point to a charged impurity distribution with a density $n_i = 7.5 \pm 0.5 \times 10^{11}$ cm^{-2} at a distance $0.1 < d < 1$ nm below the graphene, in agreement with earlier experiments in similar conditions [5,6,26].

We performed scanning tunneling spectroscopy on the graphene sheet, at distances greater than 1 μm from the metal-graphene interface as to rule out any possible influence of the leads on local properties. Figure 1(c) shows the differential tunneling conductance $G_t(V_b)$ acquired at a given location, but at different gate voltages V_g. A V-shape spectrum, characteristic of graphene, is obtained in every case. A frequently reported gate-independent depression of the tunneling conductance is seen at zero bias [21,28,29]. In addition, the curves display two gate-dependent local minima, highlighted by red and black arrows, respectively, which move in opposite directions with V_g.

The primary minimum V_b^0 (red arrows) occurs when the Fermi level of the tip is aligned with the local Dirac point $E_D(\mathbf{r})$ of graphene, which can be written as

$$V_b^0 = -\gamma \text{sgn}(V_g - V_g^D)\sqrt{|V_g - V_g^D|}, \tag{1}$$

where $\gamma = \hbar v_F \sqrt{\pi\kappa\epsilon_0/(e^3 t)}$ employing a plate-capacitor model, with $v_F = 1.1 \times 10^6$ m/s the graphene Fermi velocity, and $t = 285$ nm and $\kappa = 3.9$ the SiO_2 thickness and dielectric constant, respectively (details are described in the Supplemental Material [10]). The local quantity V_g^D is the gate voltage at which the Fermi levels of both the graphene and the tip are aligned with the Dirac point. It includes the influence of the local gating produced by the tip due to both the tip-sample work function mismatch and the bias voltage [9,30]. In the absence of capacitive coupling to the tip, the spatially averaged V_g^D would coincide with V_g^0 found from transport experiments. In the case of Fig. 1, the experimental gate dependence of the primary minimum V_b^0 can be well fitted with Eq. (1), yielding $V_g^D = 28$ V [Fig. 1(d)], the value of γ being determined by known parameters. The nearly exact matching of V_g^D at that particular position and tip

condition with the global value of V_g^0 is coincidental, since V_g^D depends on the position. The secondary minimum (black arrows in Fig. 1(c)) occurs when the Fermi level of graphene passes through the Dirac point [9,29–31]. The above analysis provides a detailed understanding of the electron tunneling spectra dependence on the gate potential, at a given location.

Several strategies can be used for mapping the local Dirac point. Performing a complete spectrum with an open feedback loop at each position, from which E_D is then individually extracted, is the most reliable method, but it is very time-consuming [2,21]. Mapping G_t with a closed feedback loop set to a fixed set-point tunnel current $I_t^{\rm set}$ and a single V_b that is slightly offset from the average primary minimum V_b^0 by δV_b was shown to reproduce qualitatively the $E_D(x,y)$ maps [2]. This stems from the fact that, to first approximation, a shift in E_D simply shifts the $G_t(V_b)$ curves along the V_b axis. Complications with this approach arise when one wishes to compare E_D maps at different gate voltages because V_b^0 itself is a function of V_g. Our strategy consists of first determining $V_b^0(V_g)$ at a given position [Fig. 1(d)] and then mapping G_t at a gate-dependent bias voltage $V_b(V_g) = V_b^0(V_g) \pm 100$ mV. The sign of the offset is set such that $|V_b| > |V_b^0|$.

We further normalize the differential tunnel conductance maps to the set-point tunnel conductance, writing $\tilde{G}_t = (V_b/I_t^{\rm set})G_t$. This normalization is known to provide a more faithful conversion of the differential tunnel conductance to the density of states when the set-point tunnel conductance is not fixed from map to map [32]. We have verified the structures observed in $\tilde{G}_t$ maps to be consistent with the E_D maps found from full current imaging tunneling spectroscopy (CITS) measurements, which were acquired at selected gate voltages. These full CITSs also allow for determining the proportionality factor between the $\tilde{G}_t$ and E_D maps (see Supplemental Material for a more detailed discussion [10]).

Experimental maps of the variations of $\tilde{G}_t \sim E_D$ around their spatially averaged value are shown for several gate voltages in Fig. 2. It is readily seen that not only the lateral extent, but also the amplitude of the doping inhomogeneities, gradually increase as the Fermi level approaches the Dirac point. For proper quantification of the observed inhomogeneities, we introduce the autocorrelation function of the E_D maps. Assuming rotational symmetry (which is only approximately true, due to the finite size of the maps), the latter is a function of only $r = |\mathbf{r}|$. The charge puddles' size ξ is determined from fitting the angular average of the autocorrelation function of each E_D map to a Gaussian decay. The gate dependence of ξ displayed in Fig. 3(a) shows a strong increase near charge neutrality, which is found at a gate voltage $\bar{V}_g^D$ of about 38 V. This value is a spatially averaged property of the map area. Because of the capacitive influence of the tip [33], $\bar{V}_g^D$ is somewhat larger than the charge neutrality condition $V_g^0 = 29$ V found from transport experiments [9,30].

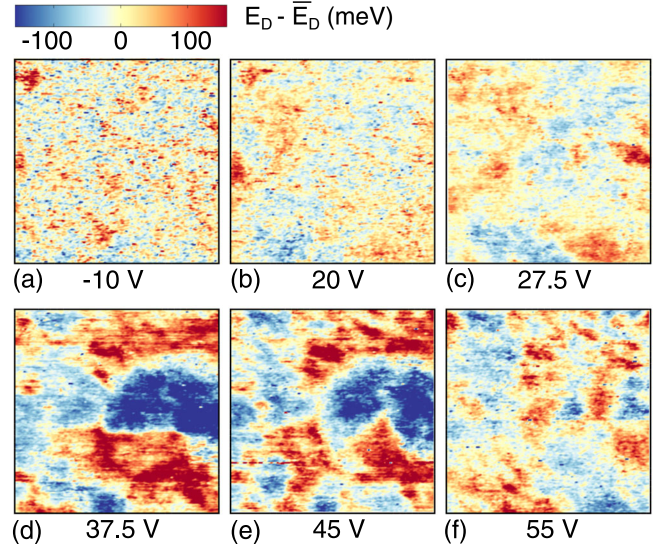

FIG. 2. Spatial maps of the variations of the local Dirac point energy E_D around its spatially averaged value $\bar{E}_D$, over an area of 100×100 nm^2 at different gate voltages (indicated below each figure). The imaging parameters for the original G_t maps (see text) are $I_t^{\rm set} = 50$ pA and bias voltages V_b equal to (a) 0.298 V, (b) 0.191 V (c) 0.122 V, (d) −0.145 V, (e) −0.232 V, and (f) −0.267 V.

We further determine the standard deviation of the Dirac point variations δE_D over a map. This quantity, which reflects the amplitude of the doping inhomogeneities across the sample, is plotted in Fig. 3(b) as a function of V_g and also shows a marked peak at $\bar{V}_g^D \approx 38$ V. The error bars on ξ and δE_D are mainly associated with the finite size of the maps; a detailed discussion of their determination can be found in the Supplemental Material [10]. Some asymmetry of the puddles' behavior is observed, which appear somewhat larger and more prominent at large electron doping, than on the hole doped side. As electron doping involves a quite large gate potential of about 60 V, a possible scenario for this asymmetry is that the back gate eventually influences the substrate impurities distribution itself [6].

Our main experimental findings are thus that both the amplitude and the spatial extent of the puddles significantly increase as the Fermi level approaches the Dirac point. For a quantitative understanding, we now compare these results to calculations. From Thomas-Fermi theory in 2D, assuming a flat Fermi sea, follows that variations in the local value of E_D/e are equal to variations in the screened electrostatic potential $\tilde{V}$ [34]. For a random 2D distribution of charged impurities with density n_i at a distance d from the graphene sheet, the autocorrelation function of the screened potential can be written [35] as

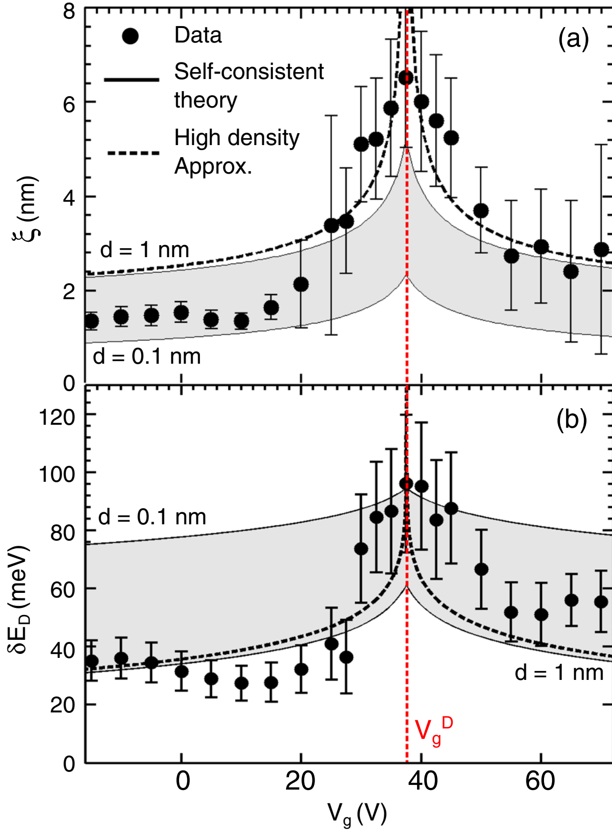

FIG. 3. (a) Puddle size and (b) amplitude of doping inhomogeneities, as a function of the back-gate potential. The dashed lines are calculations without self-consistent correction to carrier density, with $d = 1$ nm. The gray areas represent the range of values expected from a random impurity distribution at a distance d ranging from 0.1 to 1 nm from the graphene sheet. They are delimited by solid lines corresponding to calculations using the extremal values of d, respectively. For all calculations, the value derived from transport data is used: $n_i = 7.5 \times 10^{11}$ cm^{-2}.

$$C(r) = 2\pi n_i \left(\frac{e^2}{4\pi\epsilon_0\kappa}\right)^2 \int_0^{+\infty} qdq \left[\frac{1}{\epsilon(q)} \frac{e^{-qd}}{q}\right]^2 J_0(qr), \quad (2)$$

where J_0 is the zeroth-order Bessel function and $\epsilon(q)$ is the graphene dielectric function. The latter describes the screening of Dirac fermions which, within random phase approximation (RPA), can be written as [26]

$$\epsilon(q) = \begin{cases} 1 + 4k_F r_s/q & \text{for } q < 2k_F \\ 1 + \pi r_s/2 & \text{for } q > 2k_F, \end{cases} \quad (3)$$

where $r_s = e^2/(4\pi\epsilon_0\kappa\hbar v_F) \approx 0.8$ on SiO_2 is the effective fine structure constant of graphene. The dependence of the correlation function on the mean doping level (and thus on the gate potential) enters here through the dependence of $\epsilon(q)$ on $2k_F$.

We calculated the autocorrelation function for the screened potential and extracted the correlation length ξ and fluctuation amplitude $\delta\tilde{V} = \delta E_D/e$. The result for $d = 1$ nm, shown as dashed curves in Figs. 3(a) and 3(b), accounts for the overall decrease of both ξ and δE_D, that is, stronger screening with increasing charge carrier density. The calculations have no other adjustable parameter than $\bar{V}_g^D = 38$ V, the impurity density in the substrate n_i being determined from the transport measurements. The puddles' size follows, in particular, the expected trend $\xi \sim q_{\mathrm{TF}}^{-1} \propto 1/\sqrt{n}$ at high carrier densities, where $n \propto |V_g - \bar{V}_g^D|$ is the gate-induced charge carrier density. This agreement validates the microscopic picture of random potential fluctuations, for the description of which we call for Thomas-Fermi screening in a Dirac material.

At charge neutrality, for a homogeneous system, there are no excess charges available to screen the impurity potential. Accordingly, Eq. (3) predicts that both the amplitude and the correlation length diverge. However, this ignores the fact that the induced charges within the puddles can themselves screen the impurity potential. Accounting for this process self-consistently [26] leads to rewriting the RPA dielectric function of Eq. (3) with a corrected charge carrier density. The usual expression of $k_F = \sqrt{\pi n}$ is then replaced by $\sqrt{\pi(n + n^*)}$ [35], where n^* represents the disorder-induced residual charge carrier density in the graphene sheet which cannot be compensated by a global gate. The self-consistent calculations are plotted in Figs. 3(a) and 3(b). The gray regions are delimited by the theoretical curves for $d = 0.1$ and 1 nm, respectively. The ensuing saturation of both the puddles' size and amplitude at the charge neutrality point is in very good agreement with the experimentally observed trend.

To conclude, this work provides the first microscopic observation of the growth of charge inhomogeneities in graphene near the Dirac point. It further shows that the observed behavior can be very well described with a theory based on a microscopic description of the impurity potential, using parameters found from transport measurements, performed *in situ* on the very same graphene sample. This observation gives utmost credit to the charged impurity potential scenario as a limiting factor to the exploitability of Dirac physics in graphene on SiO_2 [10].

This work was funded by the European Commission under Project No. 264034 (Q-NET Marie Curie Initial Training Network). Work in Singapore was supported by the National Research Foundation of Singapore under its Fellowship program (NRF-NRFF2012-01). Samples were fabricated at the Nanofab facility at Institut Néel. We thank S. C. Martin, B. Sacépé, A. de Cecco, J. Seidemann, G. Shaw, and A. K. Gupta for discussions and help with the experiments.

*clemens.winkelmann@neel.cnrs.fr

[1] J. Martin, N. Akerman, G. Ulbricht, T. Lohmann, J. H. Smet, K. von Klitzing, and A. Yacoby, Nat. Phys. 4, 144 (2008).

[2] Y. Zhang, V. W. Brar, C. Girit, A. Zettl, and M. F. Crommie, Nat. Phys. **5**, 722 (2009).
[3] A. Deshpande, W. Bao, F. Miao, C. N. Lau, and B. J. LeRoy, Phys. Rev. B **79**, 205411 (2009).
[4] A. Deshpande, W. Bao, Z. Zhao, C. N. Lau, and B. J. LeRoy, Phys. Rev. B **83**, 155409 (2011).
[5] J.-H. Chen, C. Jang, S. Adam, M. S. Fuhrer, E. D. Williams, and M. Ishigami, Nat. Phys. **4**, 377 (2008).
[6] Y.-W. Tan, Y. Zhang, K. Bolotin, Y. Zhao, S. Adam, E. H. Hwang, S. Das Sarma, H. L. Stormer, and P. Kim, Phys. Rev. Lett. **99**, 246803 (2007).
[7] S. Das Sarma, S. Adam, E. H. Hwang, and E. Rossi, Rev. Mod. Phys. **83**, 407 (2011).
[8] K. S. Novoselov, A. K. Geim, S. V. Morozov, D. Jiang, Y. Zhang, S. V. Dubonos, I. V. Grigorieva, and A. A. Firsov, Science **306**, 666 (2004).
[9] S. K. Choudhary and A. K. Gupta, Appl. Phys. Lett. **98**, 102109 (2011).
[10] See Supplemental Material at http://link.aps.org/supplemental/10.1103/PhysRevLett.116.126804, which includes Refs. [11–20], for a description of the sample fabrication, details of the STM and transport data analysis, a derivation of the tip gating effect as well as a discussion of the Dirac point mapping procedure.
[11] K. Nagashio, T. Yamashita, T. Nishimura, K. Kita, and A. Toriumi, J. Appl. Phys. **110**, 024513 (2011).
[12] A. C. Ferrari, J. C. Meyer, V. Scardaci, C. Casiraghi, M. Lazzeri, F. Mauri, S. Piscanec, D. Jiang, K. S. Novoselov, S. Roth *et al.*, Phys. Rev. Lett. **97**, 187401 (2006).
[13] J. Yan, Y. Zhang, P. Kim, and A. Pinczuk, Phys. Rev. Lett. **98**, 166802 (2007).
[14] A. Das, S. Pisana, B. Chakraborty, S. Piscanec, S. K. Saha, U. V. Waghmare, K. S. Novoselov, H. R. Krishnamurthy, A. K. Geim, A. C. Ferrari *et al.*, Nat. Nanotechnol. **3**, 210 (2008).
[15] W. Zhu, V. Perebeinos, M. Freitag, and P. Avouris, Phys. Rev. B **80**, 235402 (2009).
[16] E. J. H. Lee, K. Balasubramanian, R. T. Weitz, M. Burghard, and K. Kern, Nat. Nanotechnol. **3**, 486 (2008).
[17] B. Huard, N. Stander, J. A. Sulpizio, and D. Goldhaber-Gordon, Phys. Rev. B **78**, 121402(R) (2008).
[18] E. Rossi, S. Adam, and S. Das Sarma, Phys. Rev. B **79**, 245423 (2009).
[19] A. H. Castro Neto, F. Guinea, N. M. R. Peres, K. S. Novoselov, and A. K. Geim, Rev. Mod. Phys. **81**, 109 (2009).
[20] Y.-J. Yu, Y. Zhao, S. Ryu, L. E. Brus, K. S. Kim, and P. Kim, Nano Lett. **9**, 3430 (2009).
[21] S. C. Martin, S. Samaddar, B. Sacépé, A. Kimouche, J. Coraux, F. Fuchs, B. Grévin, H. Courtois, and C. B. Winkelmann, Phys. Rev. B **91**, 041406 (2015).
[22] S. Heike and T. Hashizume, Appl. Phys. Lett. **83**, 3620 (2003).
[23] T. An, T. Nishio, T. Eguchi, M. Ono, A. Nomura, K. Akiyama, and Y. Hasegawa, Rev. Sci. Instrum. **79**, 033703 (2008).
[24] T. Quaglio, F. Dahlem, S. Martin, A. Gérardin, C. B. Winkelmann, and H. Courtois, Rev. Sci. Instrum. **83**, 123702 (2012).
[25] H. le Sueur, P. Joyez, H. Pothier, C. Urbina, and D. Estève, Phys. Rev. Lett. **100**, 197002 (2008).
[26] S. Adam, E. H. Hwang, V. M. Galitski, and S. Das Sarma, Proc. Natl. Acad. Sci. U.S.A. **104**, 18392 (2007).
[27] D. S. Novikov, Appl. Phys. Lett. **91**, 102102 (2007).
[28] A. Luican, G. Li, and E. Y. Andrei, Phys. Rev. B **83**, 041405 (2011).
[29] S. Jung, G. M. Rutter, N. N. Klimov, D. B. Newell, I. Calizo, A. R. Hight-Walker, N. B. Zhitenev, and J. A. Stroscio, Nat. Phys. **7**, 245 (2011).
[30] Y. Zhao, J. Wyrick, F. D. Natterer, J. F. Rodriguez-Nieva, C. Lewandowski, K. Watanabe, T. Taniguchi, L. S. Levitov, N. B. Zhitenev, and J. A. Stroscio, Science **348**, 672 (2015).
[31] J. Chae, S. Jung, A. F. Young, C. R. Dean, L. Wang, Y. Gao, K. Watanabe, T. Taniguchi, J. Hone, K. L. Shepard *et al.*, Phys. Rev. Lett. **109**, 116802 (2012).
[32] R. Wiesendanger, *Scanning Probe Microscopy and Spectroscopy* (Cambridge University Press, Cambridge, England, 1994), pp. 147.
[33] The capacitive lever arm of the tip with respect to the back gate can be estimated to $\beta \approx 50$, meaning that a tip-sample work function difference by 0.2 eV will induce a shift in V_g^D by 10 V. The determination of β is described in detail in the Supplemental Material file [10].
[34] N. W. Ashcroft and N. Mermin, *Solid State Physics* (Saunders College, Philadelphia, PA, 1976), pp. 340–342.
[35] S. Adam, S. Jung, N. N. Klimov, N. B. Zhitenev, J. A. Stroscio, and M. D. Stiles, Phys. Rev. B **84**, 235421 (2011).